39th AIAA Fluid Dynamics Conference
22 - 25 June 2009, San Antonio, Texas

AIAA 2009-4015

Detached-Eddy Simulation of a Co-Flow Jet Airfoil at High Angle of Attack

Baoyuan Wang[*], Ge-Cheng Zha[†]
Dept. of Mechanical and Aerospace Engineering
Miami Wind^{TM}
University of Miami
Coral Gables, Florida 33124
E-mail: gzha@miami.edu

Abstract

A detached-eddy simulation (DES) of a co-flow jet (CFJ) airfoil at high angles of attack (AoA) is conducted in this paper. A low diffusion E-CUSP (LDE) scheme with an implicit fifth-order WENO scheme is employed. DES appears to handle the turbulence mixing and flow separation significantly better at high AoA than RANS.

1 Introduction

To improve aircraft performance, innovative technology should be pursued to drastically reduce the weight and fuel consumption of the aircraft and to significantly increase aircraft mission payload and stall margin. Both military and commercial aircraft will benefit from the same technology. Flow control (FC) is the most promising route to bring significant performance improvement to aircraft[1, 2, 3, 4, 5, 6, 7]. Recently, Zha et al. have developed a promising airfoil flow control technique using a co-flow jet[8, 9, 10, 11], which significantly increases lift, stall margin, and drag reduction.

The co-flow jet airfoil is designed with an injection slot near leading edge and a suction slot near trailing edge on the airfoil suction surface. The slots are opened by translating a large portion of the suction surface downward. A high energy jet is injected tangentially near leading edge and the same amount of mass flow is drawn in near trailing edge. The turbulent shear layer between the main flow and the jet causes strong turbulence diffusion and mixing under the severe adverse pressure gradient, which enhances lateral transport of energy from the jet to the main flow and allows the main flow to overcome the severe adverse pressure gradient and remain attached at high angle of attack(AoA). The high energy jet induces high circulation and hence generates high lift. The energized main flow fills the wake and therefore reduces drag. The CFJ airfoil achieves net-zero mass-flux flow control and can significantly reduce the penalty to the propulsion system by dumping zero jet mass flow.

---

[*] Ph.D.

[†] Associate Professor, AIAA Senior Member, Director of Miami Wind^{TM}

In [11], the CFJ airfoils with three different slot sizes are computed using Spalart-Allmaras (S-A) model. It is observed that at low AoA, the computed results agree well with the experiment. But at high AoA, the deviation of the lift and drag is large because a RANS model is not able to simulate the flow separation accurately. In particular, the predicted stall AoA by RANS is significantly smaller than the measured one.

To overcome the disadvantages of RANS models, and to avoid the intensive CPU requirement for LES, Spalart et al. developed the detached-eddy simulation (DES) strategy[12], which is a hybrid RANS and LES method. Near the solid surface within the wall boundary layer, the unsteady RANS model is realized. Away from the wall surface, the model automatically converts to LES. By using the RANS model near the wall, the mesh size as well as the CPU time can be tremendously reduced. By using the LES model away from the wall, the regions of massive separation and other free shear flows are properly simulated. Its application for turbulence simulation has already achieved encouraging success as shown in the work of Tarvin et al. (1999)[13], Spalart (2001)[14, 15], Forsythe et al. (2002)[16], Viswanathan et al. [17], Squires et al. [18, 19], Hsnsen, et al. (2003)[20], Subbareddy et al. (2005)[21], Wang et al. (2008)[22, 23]. These flows using DES include those for airfoils, cylinders, forbodies, base flows, etc. The results are qualitatively and quantitatively better than the solutions using RANS.

The objective of this paper is to simulate the flow field of CFJ airfoil at high AoA using DES in order to better capture the jet mixing and flow separation. A low diffusion E-CUSP scheme [24, 25] with fifth-order WENO scheme[26, 27] is employed for the inviscid fluxes. The computed lifts at $AoA = 30°, 37°, 39°$ agree better with the experiment than those using S-A one equation RANS. The computed drag using DES is also improved greatly, even though the deviation remains very large. The computed stall AoA using DES is 37°, which agrees very well with the experiment and is much better than the one using S-A one equation RANS. The computed results using DES show significantly improvements at high AoA compared with those using S-A one equation RANS.

2 Governing Equations

The governing equations for the flow field computation are the spatially filtered 3D general Navier-Stokes equations in generalized coordinates and can be expressed as the following:

$$\frac{\partial \mathbf{Q}'}{\partial t} + \frac{\partial \mathbf{E}'}{\partial \xi} + \frac{\partial \mathbf{F}'}{\partial \eta} + \frac{\partial \mathbf{G}'}{\partial \zeta} = \frac{1}{\mathrm{Re}} \left(\frac{\partial \mathbf{E}'_{\mathbf{v}}}{\partial \xi} + \frac{\partial \mathbf{F}'_{\mathbf{v}}}{\partial \eta} + \frac{\partial \mathbf{G}'_{\mathbf{v}}}{\partial \zeta} \right) \tag{1}$$

where Re is the Reynolds number, and

$$\mathbf{Q}' = \frac{\mathbf{Q}}{J} \tag{2}$$

$$\mathbf{E}' = \frac{1}{J}(\xi_t \mathbf{Q} + \xi_x \mathbf{E} + \xi_y \mathbf{F} + \xi_z \mathbf{G}) \tag{3}$$

$$\mathbf{F}' = \frac{1}{J}(\eta_t \mathbf{Q} + \eta_x \mathbf{E} + \eta_y \mathbf{F} + \eta_z \mathbf{G}) \tag{4}$$

$$\mathbf{G}' = \frac{1}{J}(\zeta_t \mathbf{Q} + \zeta_x \mathbf{E} + \zeta_y \mathbf{F} + \zeta_z \mathbf{G}) \tag{5}$$

$$\mathbf{E}'_\mathbf{v} = \frac{1}{J}(\xi_x \mathbf{E}_\mathbf{v} + \xi_y \mathbf{F}_\mathbf{v} + \xi_z \mathbf{G}_\mathbf{v}) \tag{6}$$

$$\mathbf{F}'_\mathbf{v} = \frac{1}{J}(\eta_x \mathbf{E}_\mathbf{v} + \eta_y \mathbf{F}_\mathbf{v} + \eta_z \mathbf{G}_\mathbf{v}) \tag{7}$$

$$\mathbf{G}'_\mathbf{v} = \frac{1}{J}(\zeta_x \mathbf{E}_\mathbf{v} + \zeta_y \mathbf{F}_\mathbf{v} + \zeta_z \mathbf{G}_\mathbf{v}) \tag{8}$$

where J is the transformation Jacobian. The variable vector $\mathbf{Q}$, and inviscid flux vectors $\mathbf{E}$, $\mathbf{F}$, and $\mathbf{G}$ are given as the following.

$$\mathbf{Q} = \begin{pmatrix} \bar\rho \\ \bar\rho\tilde u \\ \bar\rho\tilde v \\ \bar\rho\tilde w \\ \bar\rho\tilde e \end{pmatrix}, \mathbf{E} = \begin{pmatrix} \bar\rho\tilde u \\ \bar\rho\tilde u^2 + \bar p \\ \bar\rho\tilde u\tilde v \\ \bar\rho\tilde u\tilde w \\ (\bar\rho\tilde e + \bar p)\tilde u \end{pmatrix}, \mathbf{F} = \begin{pmatrix} \bar\rho\tilde v \\ \bar\rho\tilde v\tilde u \\ \bar\rho\tilde v^2 + \bar p \\ \bar\rho\tilde v\tilde w \\ (\bar\rho\tilde e + \bar p)\tilde v \end{pmatrix}, \mathbf{G} = \begin{pmatrix} \bar\rho\tilde w \\ \bar\rho\tilde w\tilde u \\ \bar\rho\tilde w\tilde v \\ \bar\rho\tilde w^2 + \bar p \\ (\bar\rho\tilde e + \bar p)\tilde w \end{pmatrix}$$

The inviscid fluxes in generalized coordinate system are expressed as:

$$\mathbf{E}' = \begin{bmatrix} \bar\rho U \\ \bar\rho\tilde u U + l_x \bar p \\ \bar\rho\tilde v U + l_y \bar p \\ \bar\rho\tilde w U + l_z \bar p \\ (\bar\rho\tilde e + \bar p)\, U - l_t \bar p \end{bmatrix}, \ \mathbf{F}' = \begin{bmatrix} \bar\rho V \\ \bar\rho\tilde u V + m_x \bar p \\ \bar\rho\tilde v V + m_y \bar p \\ \bar\rho\tilde w V + m_z \bar p \\ (\bar\rho\tilde e + \bar p)\, V - m_t \bar p \end{bmatrix}, \ \mathbf{G}' = \begin{bmatrix} \bar\rho W \\ \bar\rho\tilde u W + n_x \bar p \\ \bar\rho\tilde v W + n_y \bar p \\ \bar\rho\tilde w W + n_z \bar p \\ (\bar\rho\tilde e + \bar p)\, W - n_t \bar p \end{bmatrix}$$

where U, V and W are the contravariant velocities in ξ, η and ζ directions.

$$\begin{aligned} U &= l_t + \mathbf{l} \bullet \mathbf{V} = l_t + l_x \tilde u + l_y \tilde v + l_z \tilde w \\ V &= m_t + \mathbf{m} \bullet \mathbf{V} = m_t + m_x \tilde u + m_y \tilde v + m_z \tilde w \\ W &= n_t + \mathbf{n} \bullet \mathbf{V} = n_t + n_x \tilde u + n_y \tilde v + n_z \tilde w \end{aligned} \tag{9}$$

$\mathbf{l}$, $\mathbf{m}$, $\mathbf{n}$ are the normal vectors on ξ, η, ζ surfaces with their magnitudes equal to the elemental surface area and pointing to the directions of increasing ξ, η, ζ.

$$\mathbf{l} = \frac{\nabla\xi}{J}, \ \mathbf{m} = \frac{\nabla\eta}{J}, \ \mathbf{n} = \frac{\nabla\zeta}{J} \tag{10}$$

$$l_t = \frac{\xi_t}{J}, \ m_t = \frac{\eta_t}{J}, \ n_t = \frac{\zeta_t}{J} \tag{11}$$

The viscous fluxes $\mathbf{E_v}$, $\mathbf{F_v}$, $\mathbf{G_v}$ are expressed as:

$$\mathbf{E_v} = \begin{pmatrix} 0 \\ \bar\tau_{xx} + \sigma_{xx} \\ \bar\tau_{xy} + \sigma_{xy} \\ \bar\tau_{xz} + \sigma_{xz} \\ Q_x \end{pmatrix}, \mathbf{F_v} = \begin{pmatrix} 0 \\ \bar\tau_{yx} + \sigma_{yx} \\ \bar\tau_{yy} + \sigma_{yy} \\ \bar\tau_{yz} + \sigma_{yz} \\ Q_y \end{pmatrix}, \mathbf{G_v} = \begin{pmatrix} 0 \\ \bar\tau_{zx} + \sigma_{zx} \\ \bar\tau_{zy} + \sigma_{zy} \\ \bar\tau_{zz} + \sigma_{zz} \\ Q_z \end{pmatrix},$$

The overbar denotes a regular filtered variable, and the tilde is used to denote the Favre filtered variable. In above equations, ρ is the density, u, v, w are the Cartesian velocity components in x, y, z directions, p is the static pressure, and e is the total energy per unit mass.

The $\bar{\tau}$ is the molecular viscous stress tensor and is estimated as:

$$\bar{\tau}_{ij} = \frac{2}{3}\tilde{\mu}\frac{\partial \tilde{u}_k}{\partial x_k}\delta_{ij} + \tilde{\mu}\left(\frac{\partial \tilde{u}_i}{\partial x_j} + \frac{\partial \tilde{u}_j}{\partial x_i}\right), \qquad i, j = 1, 2, 3 \tag{12}$$

The above equation is in tensor form, where the subscript 1, 2, 3 represent the coordinates, x, y, z, and the Einstein summation convention is used.

The molecular viscosity $\tilde{\mu} = \tilde{\mu}(\tilde{T})$ is determined by Sutherland law.

The σ is the subgrid scale stress tensor due to the filtering process and is expressed as:

$$\sigma_{ij} = -\bar{\rho}(\widetilde{u_i u_j} - \tilde{u}_i \tilde{u}_j) \tag{13}$$

The energy flux Q is expressed as:

$$Q_i = \tilde{u}_j(\bar{\tau}_{ij} + \sigma_{ij}) - \bar{q}_i + \Phi_i \tag{14}$$

where Φ is the subscale heat flux:

$$\Phi_i = -C_p\bar{\rho}(\widetilde{u_i T} - \tilde{u}_i \tilde{T}) \tag{15}$$

The $\bar{q}_i$ is the molecular heat flux:

$$\bar{q}_i = -\frac{C_p\tilde{\mu}}{Pr}\frac{\partial \tilde{T}}{\partial x_i} \tag{16}$$

$$\bar{\rho}\tilde{e} = \frac{\bar{p}}{(\gamma - 1)} + \frac{1}{2}\bar{\rho}(\tilde{u}^2 + \tilde{v}^2 + \tilde{w}^2) + \rho k \tag{17}$$

where γ is the ratio of specific heats, ρk is the subscale kinetic energy per unit volume.

$$\rho k = \frac{1}{2}\bar{\rho}(\widetilde{u_i u_i} - \tilde{u}_i \tilde{u}_i) = -\frac{1}{2}\sigma_{ii} \tag{18}$$

In the present calculation, the ρk in Eq.(17) is omitted based on the assumption that the effect is small.

For simplicity, all the overbar and tilde in above equations will be dropped in the rest of this paper.

3 Detached Eddy Simulation

The closure of the sub-grid scale stresses and heat flux are done by employing the DES of Spalart[14, 15]. The transport equation of the Spalart-Allmaras one equation turbulence model is derived by using empiricism, dimensional analysis, Galilean invariance and selected dependence on the molecular viscosity[28]. The working variable $\tilde{\nu}$ is related to the eddy viscosity. In generalized coordinate system, the normalized conservative form of the transport equation is expressed as

$$\begin{aligned} \frac{\partial \frac{1}{J}\rho\tilde{\nu}}{\partial t} + \frac{\partial \rho\tilde{\nu}U}{\partial \xi} + \frac{\partial \rho\tilde{\nu}V}{\partial \eta} + \frac{\partial \rho\tilde{\nu}W}{\partial \zeta} &= \frac{1}{Re}\left(\frac{\partial \frac{\rho}{\sigma}\left(\nu+\tilde{\nu}\right)\left(\mathbf{l}\bullet\nabla\tilde{\nu}\right)}{\partial \xi}\right. \\ . + \frac{\partial \frac{\rho}{\sigma}\left(\nu+\tilde{\nu}\right)\left(\mathbf{m}\bullet\nabla\tilde{\nu}\right)}{\partial \eta} &+ \left.\frac{\partial \frac{\rho}{\sigma}\left(\nu+\tilde{\nu}\right)\left(\mathbf{n}\bullet\nabla\tilde{\nu}\right)}{\partial \zeta} + \frac{1}{J}S_\nu\right) \end{aligned} \tag{19}$$

where

$$\begin{aligned} S_\nu = \rho c_{b1}\left(1-f_{t2}\right)\tilde{S}\tilde{\nu} + \tfrac{1}{Re}\Big[-\rho\left(c_{w1}f_w - \tfrac{c_{b1}}{\kappa^2}f_{t2}\right)\left(\tfrac{\tilde{\nu}}{d}\right)^2 \\ +\tfrac{\rho}{\sigma}c_{b2}\left(\nabla\tilde{\nu}\right)^2 - \tfrac{1}{\sigma}\left(\nu+\tilde{\nu}\right)\nabla\tilde{\nu}\bullet\nabla\rho\Big] + Re\left[\rho f_{t1}\left(\Delta q\right)^2\right] \end{aligned} \tag{20}$$

The eddy viscosity ν_t is obtained from:

$$\nu_t = \tilde{\nu}f_{v1} \qquad f_{v1} = \frac{\chi^3}{\chi^3 + c_{v1}^3} \qquad \chi = \frac{\tilde{\nu}}{\nu} \tag{21}$$

where ν is the kinematic viscosity. The production term is:

$$\tilde{S} = S + \frac{\tilde{\nu}}{k^2d^2}f_{v2}, \qquad f_{v2} = 1 - \frac{\chi}{1+\chi f_{v1}} \tag{22}$$

where S is the magnitude of the vorticity. The function f_w is given by

$$f_w = g\left(\frac{1+c_{w3}^6}{g^6+c_{w3}^6}\right)^{1/6}, \qquad g = r + c_{w2}(r^6 - r), \qquad r = \frac{\tilde{\nu}}{\tilde{S}k^2d^2} \tag{23}$$

The function f_{t2} is given by

$$f_{t2} = c_{t3}exp\left(-c_{t4}\chi^2\right) \tag{24}$$

and the trip function f_{t1} is

$$f_{t1} = c_{t1}g_t exp\left[-c_{t2}\frac{\omega_t^2}{\Delta U^2}\left(d^2 + g_t^2d_t^2\right)\right],\ g_t = min\left(0.1, \frac{\Delta q}{\omega_t\Delta x_t}\right) \tag{25}$$

where, ω_t is the wall vorticity at the wall boundary layer trip location, d is the distance to the closest wall. d_t is the distance of the field point to the trip location, Δq is the difference of the velocities between the field point and the trip location, Δx_t is the grid spacing along the wall at the trip location.

The values of the coefficients are: $c_{b1} = 0.1355, c_{b2} = 0.622, \sigma = \frac{2}{3}, c_{w1} = \frac{c_{b1}}{k^2} + (1+c_{b2})/\sigma, c_{w2} = 0.3, c_{w3} = 2, k = 0.41, c_{v1} = 7.1, c_{t1} = 1.0, c_{t2} = 2.0, c_{t3} = 1.1, c_{t4} = 2.0.$

In DES, $c_{t1} = 0$, $c_{t3} = 0$. The distance to the nearest wall, d, is replaced by $\tilde{d}$ as

$$\tilde{d} = min(d, C_{DES}\Delta) \tag{26}$$

where Δ is the largest spacing of the grid cell in all the directions.

Within the boundary layer close to walls, $\tilde{d} = d$, hence the turbulence is simulated by the RANS mode determined by the Spalart-Allmaras model[28]. Away from the boundary layer, $\tilde{d} = C_{DES}\Delta$ is most of the cases. When the production and destruction terms of the model are balanced, the length scale $\tilde{d}$ will have a Smagorinsky-like eddy viscosity and the turbulence is simulated by the LES model. Analogous to the classical LES theory, the length scale Δ is to cascade the energy to the grid size. The coefficient $C_{DES} = 0.65$ is used as set in the homogeneous turbulence[29]. The Pr_t may take the value of 0.9 within the boundary layer for RANS mode and 0.5 for LES mode away from the wall surface.

4 The Numerical Method

4.1 The Low Diffusion E-CUSP (LDE) Scheme

The LDE scheme developed by Zha et al.[24] is employed to evaluate the inviscid fluxes. The basic idea of the LDE scheme is to split the inviscid flux into the convective flux E^c and the pressure flux E^p. With the one extra equation from the S-A model for DES, the splitting is basically the same as the original scheme for the Euler equation and is straightforward. This is an advantage over the Roe scheme, for which the eigenvectors need to be derived when any extra equation is added to the governing equations.

In generalized coordinate system, the flux $\mathbf{E}$ can be split as the following:

$$\mathbf{E}' = E^c + E^p = \begin{pmatrix} \rho U \\ \rho u U \\ \rho v U \\ \rho w U \\ \rho e U \\ \rho\tilde{\nu} U \end{pmatrix} + \begin{pmatrix} 0 \\ l_x p \\ l_y p \\ l_z p \\ p\overline{U} \\ 0 \end{pmatrix} \tag{27}$$

where, U is the contravariant velocity in ξ direction and is defined as the following:

$$U = l_t + l_x u + l_y v + l_z w \tag{28}$$

$\overline{U}$ is defined as:

$$\overline{U} = l_x u + l_y v + l_z w \tag{29}$$

The convective term, E^c is evaluated by

$$E^c = \rho U \begin{pmatrix} 1 \\ u \\ v \\ w \\ e \\ \tilde{\nu} \end{pmatrix} = \rho U f^c, \ f^c = \begin{pmatrix} 1 \\ u \\ v \\ w \\ e \\ \tilde{\nu} \end{pmatrix} \tag{30}$$

let

$$C = c\left(l_x^2 + l_y^2 + l_z^2\right)^{\frac{1}{2}} \tag{31}$$

where $c = \sqrt{\gamma RT}$ is the speed of sound. Then the convective flux at interface $i + \frac{1}{2}$ is evaluated as:

$$E_{i+\frac{1}{2}}^c = C_{\frac{1}{2}}\left[\rho_L C^+ f_L^c + \rho_R C^- f_R^c\right] \tag{32}$$

where, the subscripts L and R represent the left and right hand sides of the interface.

$$C_{\frac{1}{2}} = \frac{1}{2}\left(C_L + C_R\right),\ C^+ = \alpha_L^+\left(1 + \beta_L\right)M_L - \beta_L M_L^+ - M_{\frac{1}{2}}^+$$

$$C^- = \alpha_R^-\left(1 + \beta_R\right)M_R - \beta_R M_R^- + M_{\frac{1}{2}}^-$$

$$M_L = \frac{U_L}{C_{\frac{1}{2}}},\ M_R = \frac{U_R}{C_{\frac{1}{2}}}$$

$$\alpha_{L,R} = \frac{1}{2}\left[1 \pm sign\left(M_{L,R}\right)\right]$$

$$\beta_{L,R} = -max\left[0, 1 - int\left(\left|M_{L,R}\right|\right)\right]$$

$$M_{\frac{1}{2}}^+ = M_{\frac{1}{2}}\frac{C_R + C_L\Phi}{C_R + C_L},\ M_{\frac{1}{2}}^- = M_{\frac{1}{2}}\frac{C_L + C_R\Phi^{-1}}{C_R + C_L},\ \Phi = \frac{\left(\rho C^2\right)_R}{\left(\rho C^2\right)_L}$$

$$M_{\frac{1}{2}} = \beta_L\delta^+ M_L^- - \beta_R\delta^- M_R^+$$

$$M_{L,R}^\pm = \pm\frac{1}{4}\left(M_{L,R} \pm 1\right)^2$$

$$\delta^\pm = \frac{1}{2}\left\{1 \pm sign\left[\frac{1}{2}\left(M_L + M_R\right)\right]\right\}$$

The pressure flux, E^p is evaluated as the following

$$E_{i+\frac{1}{2}}^p = \begin{pmatrix} 0 \\ \mathcal{P}^+ p\, l_x \\ \mathcal{P}^+ p\, l_y \\ \mathcal{P}^+ p\, l_z \\ \frac{1}{2}p\left[\overline{U} + \overline{C}_{\frac{1}{2}}\right] \\ 0 \end{pmatrix}_L + \begin{pmatrix} 0 \\ \mathcal{P}^- p\, l_x \\ \mathcal{P}^- p\, l_y \\ \mathcal{P}^- p\, l_z \\ \frac{1}{2}p\left[\overline{U} - \overline{C}_{\frac{1}{2}}\right] \\ 0 \end{pmatrix}_R \tag{33}$$

The contravariant speed of sound $\overline{C}$ in the pressure vector is consistent with $\overline{U}$. It is computed based on C as the following,

$$\overline{C} = C - l_t \tag{34}$$

The use of $\overline{U}$ and $\overline{C}$ instead of U and C in the pressure vector to take into account of the grid speed so that the flux will transit from subsonic to supersonic smoothly. When the grid is stationary,

$l_t = 0$, $\overline{C} = C$, $\overline{U} = U$.

The pressure splitting coefficient is:

$$\mathcal{P}^{\pm}_{L,R} = \frac{1}{4}\left(M_{L,R} \pm 1\right)^2 \left(2 \mp M_L\right) \tag{35}$$

4.2 The Fifth-Order WENO Scheme

The interface flux, $E_{i+\frac{1}{2}} = E(Q_L, Q_R)$, is evaluated by determining the conservative variables Q_L and Q_R using fifth-order WENO scheme[27]. For example,

$$(Q_L)_{i+\frac{1}{2}} = \omega_0 q_0 + \omega_1 q_1 + \omega_2 q_2 \tag{36}$$

where

$$\begin{aligned} q_0 &= \tfrac{1}{3}Q_{i-2} - \tfrac{7}{6}Q_{i-1} + \tfrac{11}{6}Q_i \\ q_1 &= -\tfrac{1}{6}Q_{i-1} + \tfrac{5}{6}Q_i + \tfrac{1}{3}Q_{i+1} \\ q_2 &= \tfrac{1}{3}Q_i + \tfrac{5}{6}Q_{i+1} - \tfrac{1}{6}Q_{i+2} \end{aligned} \tag{37}$$

$$\omega_k = \frac{\alpha_k}{\alpha_0 + \ldots + \alpha_{r-1}} \tag{38}$$

$$\begin{aligned} &\alpha_k = \tfrac{C_k}{\epsilon + IS_k},\ k = 0, \ldots, r-1 \\ &C_0 = 0.1,\ C_1 = 0.6,\ C_2 = 0.3 \\ &IS_0 = \tfrac{13}{12}\left(Q_{i-2} - 2Q_{i-1} + Q_i\right)^2 + \tfrac{1}{4}\left(Q_{i-2} - 4Q_{i-1} + 3Q_i\right)^2 \\ &IS_1 = \tfrac{13}{12}\left(Q_{i-1} - 2Q_i + Q_{i+1}\right)^2 + \tfrac{1}{4}\left(Q_{i-1} - Q_{i+1}\right)^2 \\ &IS_2 = \tfrac{13}{12}\left(Q_i - 2Q_{i+1} + Q_{i+2}\right)^2 + \tfrac{1}{4}\left(3Q_i - 4Q_{i+1} + Q_{i+2}\right)^2 \end{aligned} \tag{39}$$

where, ϵ is originally introduced to avoid the denominator becoming zero and is supposed to be a very small number. In [27], it is observed that IS_k will oscillate if ϵ is too small and also shift the weights away from the optimum values in the smooth region. The higher the ϵ values, the closer the weights approach the optimum weights, C_k, which will give the symmetric evaluation of the interface flux with minimum numerical dissipation. When there are shocks in the flow field, ϵ can not be too large to maintain the sensitivity to shocks. In [27], $\epsilon = 10^{-2}$ is recommended as an optimized value for transonic flows with shock waves.

4.3 Implicit Time Integration

The time dependent governing equations are solved using dual time stepping method suggested by Jameson[30]. To achieve high convergence rate, the implicit pseudo time marching scheme is used with the unfactored Gauss-Seidel line relaxation. The physical temporal term is discretized implicitly using a three point, backward differencing as the following:

$$\frac{\partial \mathbf{Q}}{\partial t} = \frac{3\mathbf{Q^{n+1}} - 4\mathbf{Q^{n}} + \mathbf{Q^{n-1}}}{2\Delta t} \tag{40}$$

where $n-1$, n and $n+1$ are three sequential time levels, which have a time interval of Δt. The first-order Euler scheme is used to discretize the pseudo temporal term. The semi-discretized equations of the governing equations are finally given as the following:

$$\left[\left(\frac{1}{\Delta\tau} + \frac{1.5}{\Delta t}\right) I - \left(\frac{\partial R}{\partial \mathbf{Q}}\right)^{n+1,m}\right] \delta\mathbf{Q^{n+1,m+1}} = \mathbf{R^{n+1,m}} - \frac{\mathbf{3Q^{n+1,m}} - \mathbf{4Q^{n}} + \mathbf{Q^{n-1}}}{\mathbf{2\Delta t}} \tag{41}$$

where the $\Delta\tau$ is the pseudo time step, R is the net flux evaluated on a grid point using the fifth-order WENO scheme and the second-order central differencing scheme[27].

4.4 Jet Effects on CFJ Airfoil Performance

By using a control volume analysis, Zha et al. derived an expression for the force effect of the injection and suction jets on the CFJ airfoil[9]. Based on the Newton's third law, the momentum and pressure at the injection and suction slots produce a reactionary force, which must be taken into account in the drag and lift calculations. The expressions for these reactionary forces are given as:

$$F_{x_{cfj}} = (\dot{m}_j V_{j1} + p_{j1} A_{j1}) * cos(\theta_1 - \alpha) - \gamma(\dot{m}_j V_{j2} + p_{j2} A_{j2}) * cos(\theta_2 + \alpha) \tag{42}$$

$$F_{y_{cfj}} = (\dot{m}_j V_{j1} + p_{j1} A_{j1}) * sin(\theta_1 - \alpha) - \gamma(\dot{m}_j V_{j2} + p_{j2} A_{j2}) * sin(\theta_2 + \alpha) \tag{43}$$

Where the subscripts 1 and 2 stand for the injection and suction respectively, and θ_1 and θ_2 are the angles between the injection and suction slot's surface and a line normal to the airfoil chord[9]. The total lift and drag on the airfoil can then be expressed as:

$$D = R'_x - F_{x_{cfj}} \tag{44}$$

$$L = R'_y - F_{y_{cfj}} \tag{45}$$

Where R'_x and R'_y are the surface integral of pressure and shear stress in x (drag) and y (lift) direction. For the CFD simulation, the total lift and drag are calculated using Eqs.(44) and (45).

5 Results and Discussion

The experimental free stream Mach number is about 0.11 and the Reynolds number is about 3.8×10^5, which is in the laminar/transitional region. The different boundary conditions between the experiment and DES is that the DES simulates the airfoil in an open field with no wind tunnel walls. Such difference is a common practice of DES simulation and is expected to cause little effect on simulation accuracy. A typical 3D computational mesh is shown in Fig. 1 with 19 blocks. The total grid size is 817,152 cells. In spanwise direction, the boundary conditions are defined as periodic boundary condition. The dimensionless physical time step is $\bar{t} = 0.01$, which is defined as $\bar{t} = \frac{t}{D/U_\infty}$. The computation begins with a uniform flow field.

The focus of this research is to investigate the DES at high AoAs where the RANS solver predicts that the flow is separated and stalled. Since the DES is CPU intensive, only three AoAs are selected to conduct the simulation. They are 30°, 37° and 39°. The 30° is the stall AoA predicted by the RANS model. The 37° is the experimental AoA and 39° is the experimental AoA after the airfoil stall and has massive separation. Since DES is time accurate unsteady calculation, all the steady state results obtained are based on time average.

For both DES and RANS simulation, the momentum coefficients of the injection are matched with the experiment by adjusting injection total pressure. The mass flowrate of suction is matched with the mass flowrate of injection by adjusting the suction static pressure. Fig.2 plots the momentum coefficients vs the AoA. Both the computed momentum coefficients match the experimental values very well.

Fig. 3 shows the comparison of the lift coefficients between the experiment and those computed by RANS and DES. The RANS results agree in general reasonably well at low AoA when the flow is not near stall. The RANS model predicts the stall at AoA=30°, which is significantly smaller than the experimental stall AoA of 37°. Whereas, the DES predicts the stall AoA at 37° and in excellent agreement with the experiment. Even though the DES predicted lift coefficients are lower than the experiment, they are substantially closer to the experiment than the RANS results. At AoA of 39° after the stall, the lift coefficient computed by DES is virtually the same as the experiment. This indicates that the DES indeed handles the flow separation better than the RANS model.

Fig. 4 is the drag coefficient of the CFJ airfoil. Similar to the lift prediction, the computed drags using DES are greatly improved compared with those using DES at high AoA. However, the drags are still under-predicted compared with experiment. Again, this may be attributed to the insufficient turbulence mixing and separating simulation.

Fig.5 and 6 are the Mach number contours with streamlines of the CFJ airfoil at AoA=39°. The CFJ airfoil has a massive separation starting downstream of the injection slot. Fig.5 and 6 show that the separation is 3D and the flow is unsteady. The reason that the DES agrees better for the stall AoA is certainly partially attributed to the 3D unsteady simulation, which is closer to the reality.

Fig. 7 and 8, 9 and 10, and 11 and 12 compare the streamlines of the 2D RANS simulation and 3D DES of the mid-plane at AoA=30°,37°, and 39°. At AoA=30°, the RANS predicts the separation zone smaller than that of the DES. However, the RANS predicts the airfoil start to stall, whereas the DES predicts that the airfoil lift continues to rise and is consistent with the experiment. At AoA=37°, both experiment and DES indicate that the airfoil starts to stall. The separation pattern predicted by RANS and DES is very different at this AoA. The RANS has three recirculation zones and DES has two recirculation zones. At AoA=39°, the DES has three recirculation zone and DES has two recirculation zones.

6 Conclusions

The co-flow jet airfoil is simulated by using detached-eddy simulation at high angles of attack. A low diffusion E-CUSP scheme [24] and fifth-order WENO scheme are used for inviscid fluxes. The computed stall AoA using DES is 37°, which agrees excellently with the experiment and is much better than that using RANS. The computed lift and drag have been significantly improved by using DES compared with RANS. The computed lift agrees very well with the experiment at $AoA = 39°$, but the computed drag still is largely deviated from the experiment. DES appears to handle the turbulence mixing and flow separation at high angle of attack much better than RANS models even though quantitative solutions are still not satisfactory which RANS can not deals with well. The improvement of DES over RANS is attributed to the 3D unsteady simulation of the separated turbulent flows and the more advanced turbulence modeling.

7 Acknowledgment

This research is supported under ARO/AFOSR Grant 50827-RT-1SP monitored by John Schmisseur at AFOSR and Peggy A. Lacewell at ARO.

References

[1] W. L. I. Sellers, B. A. Singer, and L. D. Leavitt, "Aerodynamics for Revolutionary Air Vehicles." AIAA 2004-3785, June 2003.

[2] M. Gad-el Hak, "Flow Control: The Future ," *Journal of Aircraft*, vol. 38, pp. 402–418, 2001.

[3] M. Gad-el Hak, *Flow Control, Passive, Active, and Reactive Flow Management.* Cambridge University Press, 2000.

[4] S. Anders, W. L. Sellers, and A. Washburn, "Active Flow Control Activities at NASA Langley." AIAA 2004-2623, June 2004.

[5] C. P. Tilmann, R. L. Kimmel, G. Addington, and J. H. Myatt, "Flow Control Research and Application at the AFRL's Air Vehicles Directorate." AIAA 2004-2622, June 2004.

[6] D. Miller, , and G. Addington, "Aerodynamic Flowfield Control Technologies for Highly Integrated Airframe Propulsion Flowpaths." AIAA 2004-2625, June 2004.

[7] V. Kibens and W. W. Bower, "An Overview of Active Flow Control Applications at The Boeing Company." AIAA 2004-2624, June 2004.

[8] G.-C. Zha, C. Paxton, A. Conley, A. Wells, and B. Carroll, "Effect of Injection Slot Size on High Performance Co-Flow Jet Airfoil," *AIAA Journal of Aircraft*, vol. 43, no. 4, 2006.

[9] G.-C. Zha, W. Gao, and C. Paxton, "Jet Effects on Co-Flow Jet Airfoil Performance," *AIAA Journal, No. 6,*, vol. 45, pp. 1222–1231, 2007.

[10] G.-C. Zha, B. Carroll, C. Paxton, A. Conley, and A. Wells, "High Performance Airfoil with Co-Flow Jet Flow Control," *AIAA Journal*, vol. 45, 2007.

[11] B.-Y. Wang, B. Haddoukessouni, J. Levy, and G.-C. Zha, “Numerical Investigations of Injection Slot Size Effect on the Performance of Co-Flow Jet Airfoil,” *Journal of Aircraft*, vol. 45, pp. 2084–2091, No.6, 2008.

[12] P. Spalart, W.-H. Jou, M. Strelets, and S. Allmaras, “Comments on the Feasibility of LES for Wings, and on a Hybrid RANS/LES Approach.” Advances in DNS/LES, 1st AFOSR Int. Conf. on DNS/LES, Greyden Press, Columbus, H., Aug. 4-8, 1997.

[13] A. Tarvin, M. Shur, M. Strelets, and P. Spalart, “Detached-Eddy Simulations Past a Circular Cylinder,” *Flow Turbulence and Combustion*, vol. 63, 1999.

[14] P. R. Spalart, “Young-Person’s Guide to Detached-Eddy Simulation Grids.” NASA/CR-2001-211032, 2001.

[15] P. R. Spalart, “Topics in Detached-Eddy Simulation.”

[16] J. R. Forsythe, K. A. Hoffmann, and K. D. Cummings, R. M. Squires, “Detached-Eddy Simulations with Compressibility Corrections Applied to Supersonic Axisymmetric Base Flow,” *Journal of Fluids Engineering*, vol. 124, 2002.

[17] A. Viswanathan, K. Klismith, J. Forsythe, and K. D. Squires, “Detached-Eddy Simulation around a Forebody at High Angle of Attack.” AIAA-2003-0263, 2003.

[18] K. D. Squires, “Detached-Eddy Simulation: Current Status and Perspectives.”

[19] K. D. Squires, J. R. Forsythe, and P. R. Spalart, “Detached-Eddy Simulation of the Seperated Flow Around a Forebody Cross-Section.”

[20] R. P. Hansen and J. R. Forsythe, “Large and Detached Eddy Simulation of a Circular Cylinder Using Unstructured Grids.” AIAA Paper 2003-0775, Jan. 2003.

[21] P. Subbareddy and G. V. Candler, “Numerical Investigations of Supersonic Base Flows Using DES.” AIAA Paper 2005-0886, Jan. 2005.

[22] B.-Y. Wang and G.-C. Zha, “ Detached Eddy Simulations of a Circular Cylinder Using a Low Diffusion E-CUSP and High-Order WENO Scheme.” AIAA Paper 2008-3855, AIAA 38th Fluid Dynamics Conference, Seattle, Washington, June 23-26, 2008.

[23] B.-Y. Wang and G.-C. Zha, “Dettached Eddy Simulation of Transonic Airfoil Limited Cycle Oscillation with High Order WENO Scheme.” AIAA Paper 2009-1507, the 47th AIAA Aerospace Sciences Meeting and Exhibit, Orlando, Florida, 5 - 8 Jan 2009.

[24] G.-C. Zha, Y. Shen, and B. Wang, “Calculation of Transonic Flows Using WENO Method with a Low Diffusion E-CUSP Upwind Scheme.” AIAA Paper 2008-0745, 46th AIAA Aerospace Sciences Meeting, Reno, NV, Jan. 2008.

[25] B.-Y. Wang and G.-C. Zha, “Comparison of a Low Diffusion E-CUSP and the Roe Scheme for RANS Calculation.” AIAA Paper 2008-0596, 46th AIAA Aerospace Sciences Meeting and Exhibit, Jan. 7-10, 2008.

[26] C.-W. Shu, “Essentially Non-Oscillatory and Weighted Essentially Schemesfor Hyperbolic Conservation Laws.” NASA/CR-97-206253, 1997.

[27] Y.-Q. Shen, G.-C. Zha, and B.-Y. Wang, “Improvement of Stability and Accuracy for Weighted Essentially Nonoscillatory Scheme,” *AIAA Journal*, vol. 47, pp. 331–344, No.2, 2009.

[28] P. Spalart and S. Allmaras, “A One-equation Turbulence Model for Aerodynamic Flows.” AIAA-92-0439, 1992.

[29] M. Shur, P. Spalart, M. Strelets, and A. Travin, “Detached-Eddy Simulation of an Airfoil at High Angle of Attack”, 4th Int. Symp. Eng. Turb. Modelling and Measurements, Corsica.” May 24-26, 1999.

[30] A. Jameson, “Time Dependent Calculations Using Multigrid with Applications to Unsteady Flows Past Airfoils and Wings.” AIAA Paper 91-1596, 1991.

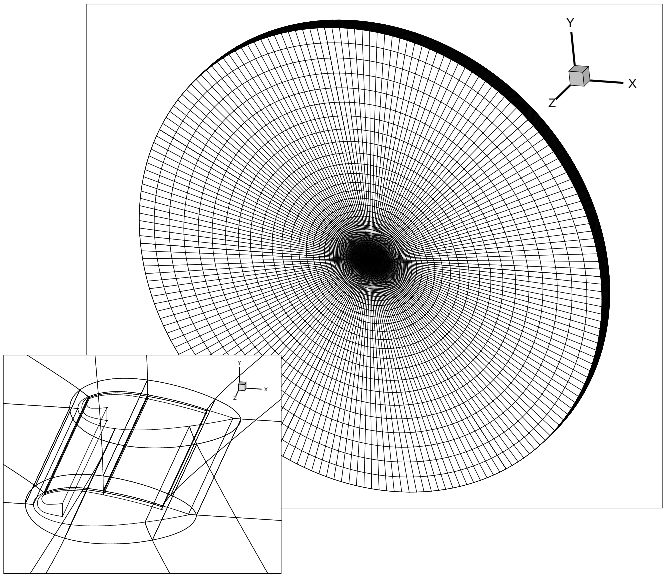

Figure 1: 19-block grids for CFJ airfoil.

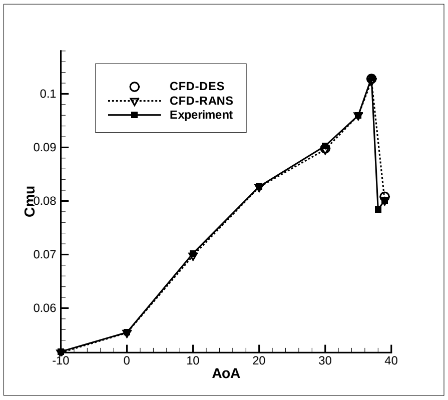

Figure 2: Injection momentum coefficient of CFJ airfoil.

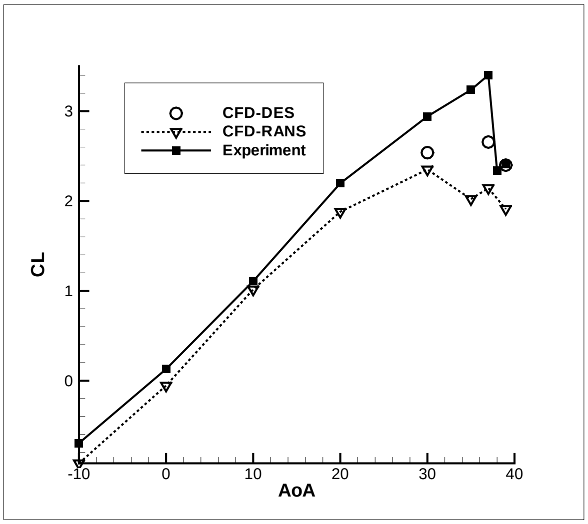

Figure 3: Lift coefficient of CFJ airfoil.

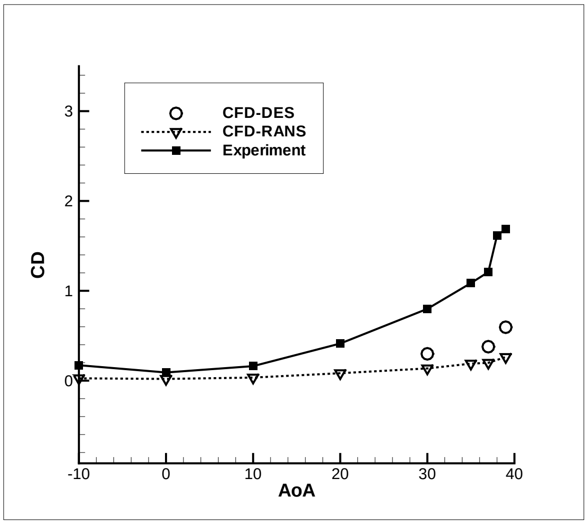

Figure 4: Drag coefficient of CFJ airfoil.

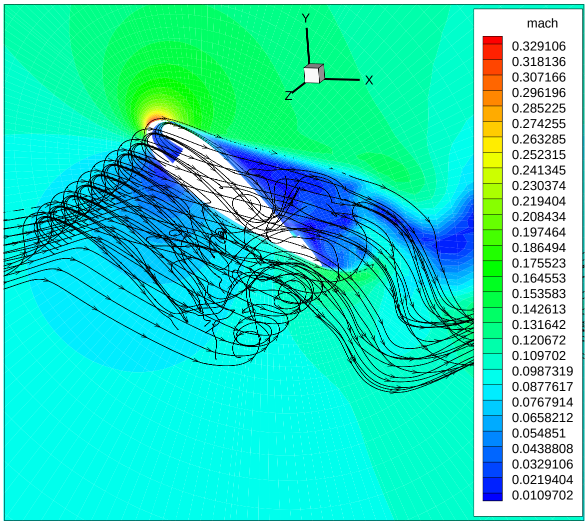

Figure 5: Mach number contours and stream lines of CFJ0025-065-196 airfoil at AoA=39°.

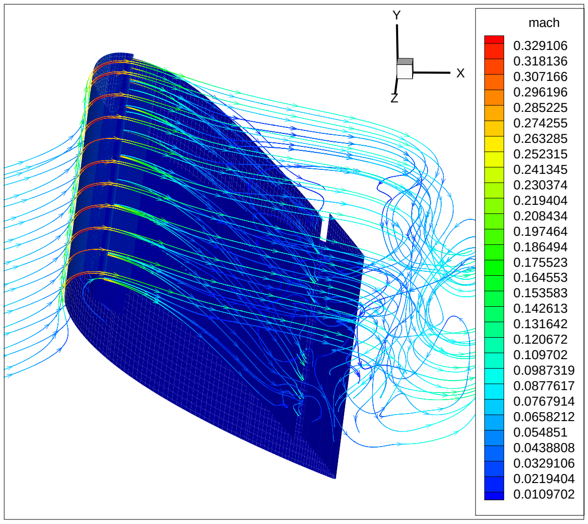

Figure 6: Stream lines on the suction surface of CFJ0025-065-196 airfoil at AoA=39°.

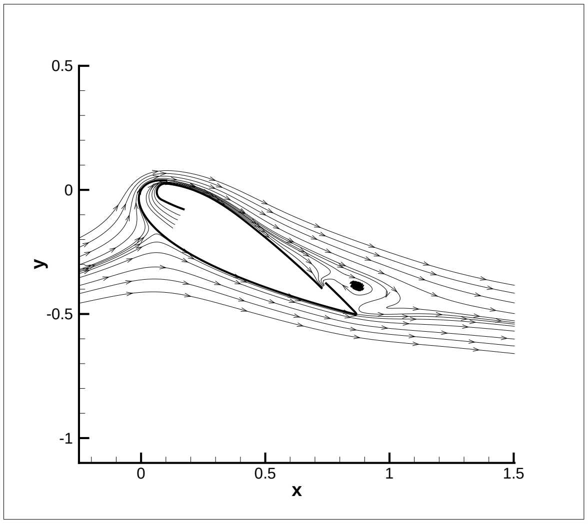

Figure 7: Streamlines predicted by RANS at AoA=30°.

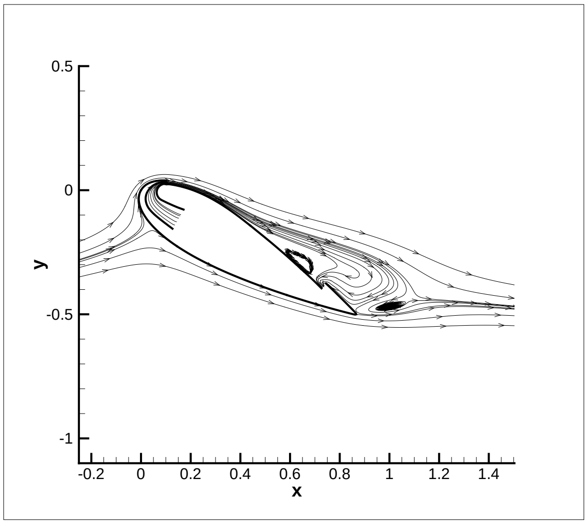

Figure 8: Streamlines predicted by DES at AoA=30°, mid-plane.

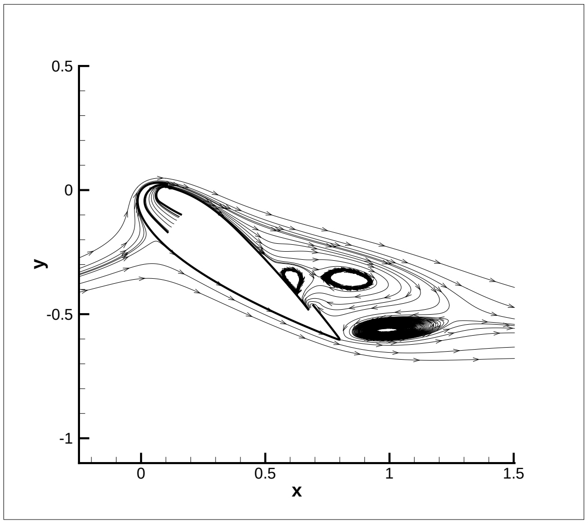

Figure 9: Streamlines predicted by RANS at AoA=37°.

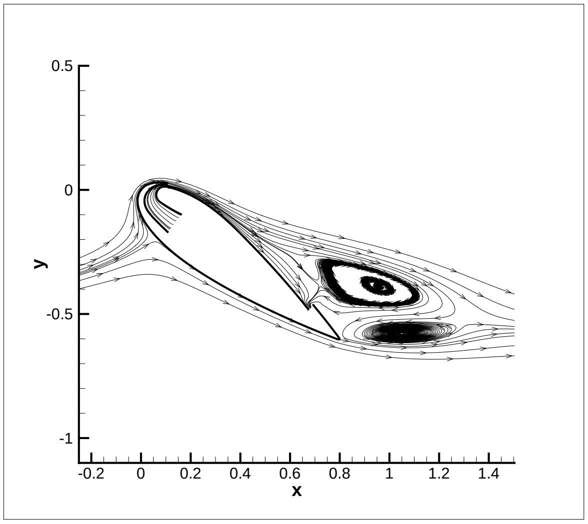

Figure 10: Streamlines predicted by DES at AoA=37°, mid-plane.

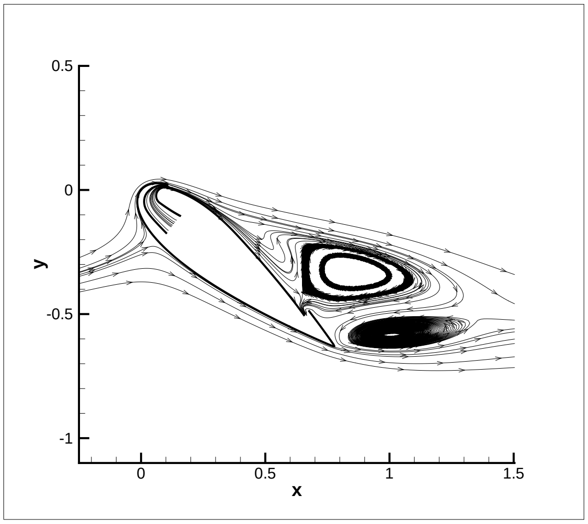

Figure 11: Streamlines predicted by RANS at AoA=39°.

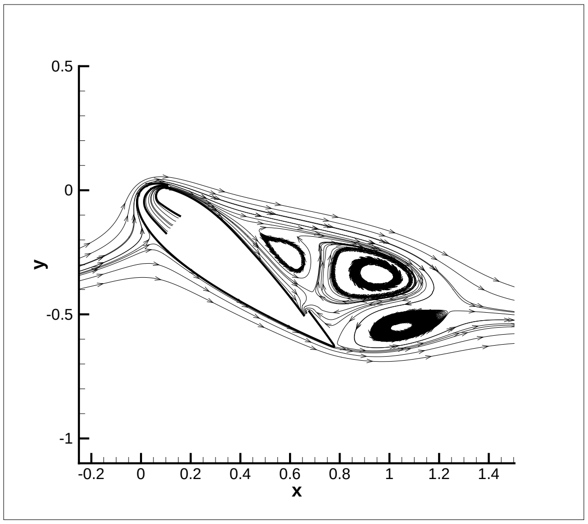

Figure 12: Streamlines predicted by DES at AoA=39°, mid-plane.